Energy Proceedings
Vol 41, 2024
ISSN 2004-2965

Enhancing the Discharge Performance of Liquid Metal Batteries through External Magnetic Fields

Xianbo Zhou [1], Kai Jiang [1], Kangli Wang [1*]

1 School of Electrical and Electronic Engineering, Huazhong University of Science and Technology, Wuhan, Hubei, 430074, China

(*Corresponding Author: klwang@hust.edu.cn)

ABSTRACT

Liquid metal batteries are considered a competitive alternative for grid-level stationary energy storage. In this study, we investigated the effects of external magnetic fields on the charge and discharge performance of this all-liquid battery composed of three layers of fluids. Experimental results indicate that, at the current density of 500 mA cm^{-2}, the application of a 100 mT magnetic field increases the discharge voltage by 34.64% compared to the case without a magnetic field. At a higher current density of 1000 mA cm^{-2}, applying a 50 mT magnetic field results in a 74.5% increase in discharge voltage, demonstrating significant effects. Furthermore, we develop a numerical model using a multiphysics simulation software to uncover the underlying mechanisms. The Lorentz force generated by the interaction of the external magnetic field and discharge current induces a swirling flow in the phi direction. At sufficiently high flow velocities, turbulent flow with a notable |z| direction component is formed, assisting the transport of Li atoms in the positive electrode, reducing concentration polarization, and thereby enhancing the discharge voltage.

Keywords: liquid metal battery, external magnetic field, turbulence, concentration polarization, discharge voltage

NONMENCLATURE

Abbreviations	
LMB	Liquid metal battery
EVF	Electro-vortex flow
MHD	Magnetohydrodynamic
MF	Magnetic field
Symbols	
a	Activity
$\boldsymbol{B}$	Magnetic induction (T)
c	Concentration (mol m^{-3})
c_p	Heat capacity (J kg^{-1} K^{-1})
D	Diffusion coefficient (cm^2 s^{-1})
E	Voltage (V)
$\boldsymbol{f}_L$	Lorentz force (N)
F	Faraday's constant (C mol^{-1})
$\boldsymbol{J}$	Current density (A m^{-2})
k	Thermal conductivity (W m^{-1} K^{-1})
k_t	Turbulent kinetic energy (m^2 s^{-2})
$\boldsymbol{N}$	Flux (mol m^{-2} s^{-1})
p	Fluid pressure (Pa)
R	Source term (mol m^{-3} s^{-1})
t	Time (s)
T	Temperature (K)
$\boldsymbol{u}$	Flow velocity (m s^{-1})
z	Charge number
φ	Potential (V)
σ	Electrical conductivity (S m^{-1})
μ	Dynamic viscosity (Pa·s)
μ_m	Electrical mobility (s mol kg^{-1})
μ_t	Turbulent viscosity (Pa·s)
ρ	Density (kg m^{-3})
ε	Turbulent dissipation rate (m^2 s^{-3})
Subscripts	
el	Electrolyte
ed	Electrode
neg	Negative electrode
pos	Positive electrode
ref	Reference value
0	Initial value

1. INTRODUCTION

With the transition of the power system towards renewable energy sources, large-scale electrochemical

This is a paper for 15th International Conference on Applied Energy (ICAE2023), Dec. 3-7, 2023, Doha, Qatar.

energy storage will play a crucial role in future power systems [1]. However, Li-ion batteries face challenges in meeting the requirements for grid-level energy storage in terms of cycling life, safety, and cost-effectiveness [2]. Liquid metal batteries (LMBs) depart from the conventional battery structure and innovatively adopt a fully-liquid design [3]. Both the negative and positive electrodes in LMBs consist of liquid metals, with an inorganic molten salt serving as the electrolyte. Due to immiscibility, the three liquid layers stratify based on density differences [4]. Liquid metal batteries completely circumvent issues such as dendrite growth, electrode structural collapse, and parasitic reactions at the electrode-electrolyte interface [5]. LMBs exhibit exceptionally long cycle life [6], high safety characteristics, and low energy storage costs, making them a highly competitive choice in the field of large-scale stationary energy storage [7–12].

Different from conventional batteries, liquid metal batteries possess a unique all-liquid structure that renders fluid flow a significant influencer on their performance and stability. A certain degree of flow can effectively enhance mass transport, elevating the discharge voltage and energy efficiency. However, too violent flow can destabilize the liquid-liquid interface, triggering short-circuits [13]. Therefore, a comprehensive understanding and utilization of fluid flow are of paramount significance for the performance optimization of LMBs [14,15].

Researches have indicated that during the charging process of LMBs, violent solutal convection spontaneously forms within the positive electrode, effectively mitigating concentration polarization [16,17]. This phenomenon arises because, during charging, Li atoms strip from the upper surface of the positive electrode, leading to an unstable density stratification with higher density in the upper layer and lower density in the lower layer, thus triggering convection. However, during the discharging process, as the lower-density Li atoms deposit onto the high-density surface of Bi and diffuse downwards, a stable density stratification emerges in the positive electrode with lighter alloy in the upper layer and denser alloy in the lower layer. This stable stratification suppresses all fluid flow in the positive electrode, resulting in a larger concentration polarization [18,19].

Therefore, some researchers have proposed the concept of generating swirl flow through an external magnetic field to facilitate mass transfer in the positive electrode during the discharge process. For instance, in 2021, Herreman et al. simulated the application of an external vertical magnetic field of 1~10 mT to a liquid metal battery, generating swirl flow that disrupted stable density stratification and significantly reduced concentration polarization [20]. In 2022, P. A. Davidson found through simulations that only a small external magnetic field is needed to trigger turbulence in the Bi positive electrode [21]. In 2023, Declan Finn Keogh et al. conducted a comparative study on the interplay between swirl flow generated by the external magnetic field and thermally stratifying buoyancy and compositional buoyancy force [22]. However, all research about the application of an external magnetic field on liquid metal batteries has been based on numerical simulations. To date, no one has experimentally validated this approach.

In this study, we have established, for the first time, the experimental platform for applying external magnetic fields to liquid metal batteries and unveiled the significant enhancement of discharge performance caused by external magnetic fields. Additionally, we developed a comprehensive and realistic model using COMSOL Multiphysics. The accuracy of the model was validated by comparing simulated discharge curves with measured ones. Finally, the model was employed to elucidate the mechanisms by which the external magnetic field improves discharge performance. This work lays the foundation for applying magnetic field technology in future LMB modules.

2. EXPERIMENT

2.1 Battery assembly

The type of LMB used in this study is Li|LiCl-KCl|Bi. For details regarding the battery assembly process of the battery, please refer to [23].

2.2 Applying external magnetic fields

The experimental setup, as presented in Fig. 1, consists of five components:

1. Helmholtz coils: Employed to apply a uniform magnetic field in the horizontal direction (x direction).

2. Liquid metal battery: Positioned in the heating furnace (3) and centrally located within the Helmholtz coils.

3. Heating furnace: Provides the suitable operating temperature (450 ^{o}C) for the LMB.

4. Thermocouple: Used for calibrating the temperature of the LMB.

5. Magnetic field control system: Automatically adjusts the current in the coils based on the set magnetic induction.

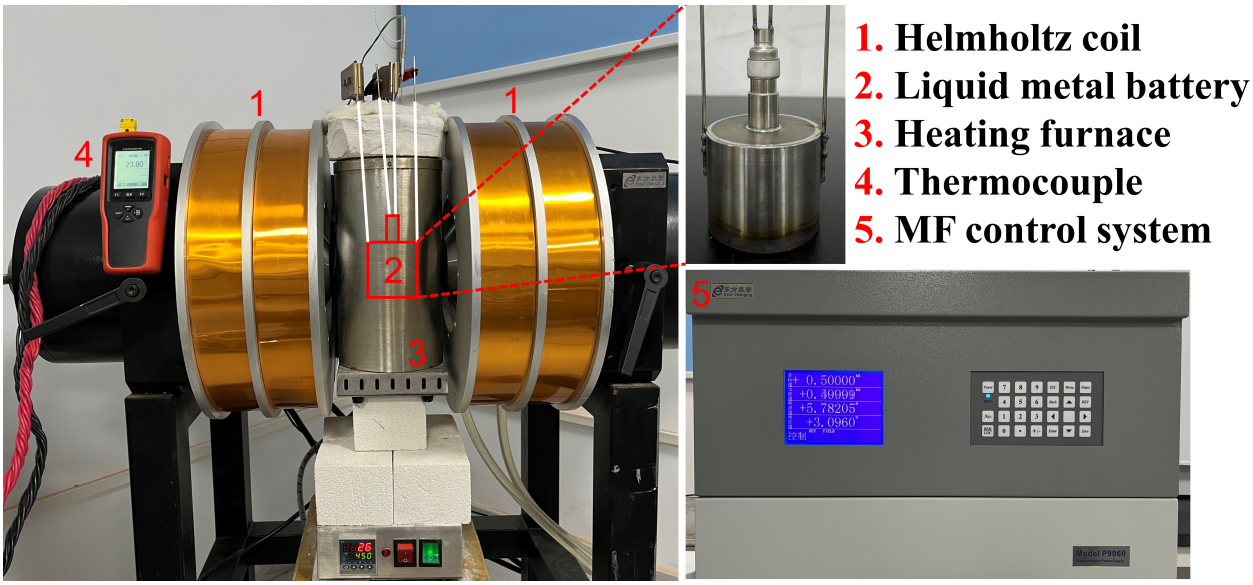

Fig. 1. Experimental platform for applying external magnetic fields to liquid metal batteries

Both the heating furnace and the liquid metal battery are made by non-magnetic materials to avoid additional influences.

3. MODEL DEVELOPMENT

3.1 Overview

A 2D rotational axisymmetric model was developed by the finite element method (FEM) software (COMSOL Multiphysics 6.0). The model incorporated four physical fields: Tertiary Current Distribution, Transport of Diluted Species, Turbulence (Realizable k-ε), and Heat Transfer in Fluids. The dimensions of the model are illustrated in Fig. 2a. The extremely fine free quadrilateral mesh was employed, with dynamic meshing set in the fluid domain (electrolyte and positive electrode). The mesh consisted of 25,059 quads with the average element quality of 0.9912. Material properties are provided in Table 1 [24].

The main assumptions of the model are as follows:

1. The 2D axisymmetric model was utilized rather than the 3D model to reduce computational complexity. The model included the negative electrode domain, positive electrode domain, and electrolyte domain, excluding components like battery leads, the heating furnace, and Helmholtz coils (Fig. 2a).

2. The MF environment in which the liquid metal battery operates was assumed to be uniform (in x direction).

3. Neglecting self-induced magnetic fields of the battery and the geomagnetic field, as they are significantly weaker compared to the applied magnetic field.

4. Liquid Li is adsorbed in the Ni-Fe foam and its flow is strictly limited. Therefore, the flow of the negative electrode was not considered.

5. Electrochemical polarization was ignored due to the ultra-fast dynamic of the liquid-liquid interface [25]. Electrochemical reaction heat was also neglected [26].

6. Volume expansion of the positive electrode was disregarded due to the short simulation time (300 s).

3.2 Governing equations and boundary conditions

The equilibrium potential of the negative and positive electrodes ($\varphi_{eq,neg}$, $\varphi_{eq,pos}$) can be expressed by the Nernst equation:

$$\varphi_{eq,neg} = \varphi^{\Theta} - \frac{RT}{nF} ln \frac{a_{Li}}{a_{Li^+}} = \frac{RT}{F} ln\, a_{Li^+} \quad (1)$$

$$\varphi_{eq,pos} = \varphi^{\Theta} - \frac{RT}{nF} ln \frac{a_{Li(in\ Bi)}}{a_{Li^+}} = -\frac{RT}{F} ln\, a_{Li(in\ Bi)} + \frac{RT}{F} ln\, a_{Li^+} \quad (2)$$

$$a_{Li^+} = \frac{c_{Li^+}}{c_{Li^+,\,ref}} = \frac{c_{Li^+}}{c_{0,\,Li^+}} \quad (3)$$

$$a_{Li(in\ Bi)} = \exp\left(-\frac{E_{eq,cell}F}{RT}\right) \quad (4)$$

In Eq. 1-2, φ^{Θ} represents the reference electrode potential for the reaction. Since this work involves only one electrochemical reaction, we assume φ^{Θ} = 0 V. R is the ideal gas constant (R = 8.314 J mol^{-1} K^{-1}), T is the temperature, n is the number of transferred electrons (n = 1), and F is Faraday's constant (F = 96485 C mol^{-1}). a_{Li} in Eq. 1 represents the activity of Li in the negative

electrode. Since the negative electrode is a pure substance, $a_{Li}=1$. a_{Li^+} represents the activity of Li ions in the molten salt electrolyte. The activity of ions in the molten salt is challenging to determine experimentally; therefore, we set it as the ratio of the local Li ion concentration (c_{Li^+}) to the reference Li ion concentration c_{ref,Li^+} (the initial Li^+ concentration c_{0,Li^+}, Eq. 3). a_{Li} in Eq. 2 denotes the activity of Li in the positive electrode. Since the equilibrium voltage ($E_{eq,cell}$) of the battery can be obtained through Coulometric titration [25], the value of a_{Li} can be calculated using Eq. 4.

The current density ($\boldsymbol{J_{ed}}$) and potential (φ_{ed}) distributions in electrodes can be calculated by Eq. 5-6:

$$\boldsymbol{J_{ed}} = -\sigma_{ed}\nabla\varphi_{ed} \tag{5}$$

$$\nabla\cdot\boldsymbol{J_{ed}} = 0 \tag{6}$$

Where, σ_{ed} is the electrode conductivity (Table 1).

The electrolyte current is generated by the movement of ions. The current density ($\boldsymbol{J_{el}}$), potential (φ_{el}), and the ion concentration (c_i) in the electrolyte satisfy the mass conservation equation (Eq. 7) and the charge conservation equation (Eq. 8):

$$\frac{\partial c_i}{\partial t} + \nabla\cdot\boldsymbol{N_i} = R_i \tag{7}$$

$$\nabla\cdot\boldsymbol{J_{el}} = F\sum_i z_i R_i \tag{8}$$

$$\boldsymbol{N_i} = -D_i\nabla c_i - z_i\mu_{m,i}Fc_i\nabla\varphi_{el} + \boldsymbol{u}c_i \tag{9}$$

$$\boldsymbol{J_{el}} = F\sum_i z_i\boldsymbol{N_i} \tag{10}$$

$$R_{Li^+} = \frac{v_{Li^+} i_{loc}}{nF} \tag{11}$$

In Eq. 7, $\boldsymbol{N_i}$ represents the flux of ion i (see Eq. 9). R_i represents the source term. For K^+ and Cl^-, there are no sources or sinks. For Li^+, taking the discharge process as an example, Li^+ is generated at the negative electrode-electrolyte interface and consumed at the positive electrode-electrolyte interface. At the electrode-electrolyte interface, R_{Li^+} can be solved using Faraday's law (Eq. 11). z_i denotes the charge number of ion i, D_i is the diffusion coefficient [27], $\mu_{m,i}$ is the electrical mobility, which can be solved using the Nernst-Einstein equation. $\boldsymbol{u}$ is the flow velocity, which will be discussed further in the following. v_{Li^+} is the stoichiometric coefficient (v_{Li^+} =1). i_{loc} represents the current density at the electrode-electrolyte interface.

The Li concentration (c_{Li}) in the positive electrode is solved by the mass conservation equation (Eq. 12):

$$\frac{\partial c_{Li}}{\partial t} + \nabla\cdot\boldsymbol{N_{Li}} = R_{Li} \tag{12}$$

$$\boldsymbol{N_{Li}} = -D_{Li}\nabla c_{Li} + \boldsymbol{u}c_{Li} \tag{13}$$

$$D_{Li} = \exp\left(\frac{-36.57x_{Li} - 4.27}{x_{Li}^2 + 3.076x_{Li} + 0.5039}\right) \tag{14}$$

$$x_{Li} = \frac{c_{Li}}{c_{Li} + c_{Bi}} \tag{15}$$

$\boldsymbol{N_{Li}}$ represents the flux of lithium in the positive electrode (Eq. 13), where R_{Li} denotes the source term, calculated using Faraday's law similar to Eq. 11. D_{Li} is the diffusion coefficient of lithium (Eq. 14), and x_{Li} is the molar fraction of lithium (Eq. 15).

The boundary conditions for the electric field are as follows: the left boundary is an axisymmetric boundary. The upper surface of the negative electrode is grounded (φ = 0 V), and the bottom surface of the positive electrode is set to a constant current density (500 mA cm^{-2} or 1000 mA cm^{-2}). A potential step is defined at the negative electrode-electrolyte interface and positive electrode-electrolyte interface (Eq. 1,2). All other boundaries are set to be electrically insulated ($-\boldsymbol{n}\cdot\boldsymbol{J}=0$).

For the concentration field, the boundary conditions are as follows: the left boundary is an axisymmetric boundary. The negative electrode-electrolyte interface and positive electrode-electrolyte interface are treated as flux boundaries ($-\boldsymbol{n}\cdot\boldsymbol{N}=R$), while all other boundaries are considered no-flux boundaries ($-\boldsymbol{n}\cdot\boldsymbol{N}=0$).

The temperature distribution (T) within the battery can be obtained by solving the heat transfer equation:

$$\rho c_p\frac{\partial T}{\partial t} + \rho c_p\boldsymbol{u}\cdot\nabla T + \nabla\cdot(-k\nabla T) = \frac{\boldsymbol{J}^2}{\sigma} \tag{16}$$

Where ρ is the density (Eq. 20-21), c_p is the constant-pressure heat capacity, $\boldsymbol{u}$ is the fluid flow velocity, k is the thermal conductivity, $\boldsymbol{J}$ is the current density, and σ is the electrical conductivity. The initial temperature (T_0) is 450 °C.

The boundary conditions for the temperature field are as follows: the left boundary is axisymmetric. The upper surface, sidewalls, and lower surface of the battery are set as natural convection boundaries with an external temperature of 450 °C, and the external fluid is air. Both the electrodes and electrolyte are defined as heat sources (Joule heating).

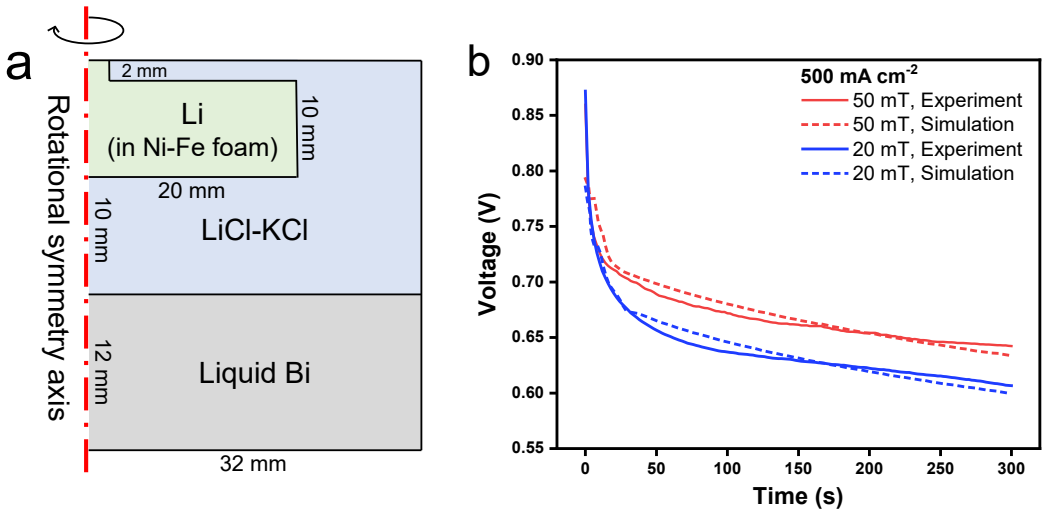

Fig. 2. (a) Dimensions of the 2D axisymmetric model.
(b) Model validation through the comparison of the measured and simulated discharge curves

The velocity $\boldsymbol{u}$ and pressure p of fluids are solved using the Realizable k-ε model:

$$\rho\frac{\partial \boldsymbol{u}}{\partial t}+\rho(\boldsymbol{u}\cdot\nabla)\boldsymbol{u}=\nabla\cdot[-p\boldsymbol{I}+\boldsymbol{K}]+\rho\boldsymbol{g}+\boldsymbol{f}_L \tag{17}$$

$$\rho\nabla\cdot\boldsymbol{u}=0 \tag{18}$$

$$\boldsymbol{f}_L=\boldsymbol{J}\times\boldsymbol{B}=\begin{vmatrix} x & phi & z \\ j_x & j_{phi} & j_z \\ B_x & 0 & 0 \end{vmatrix}=(0 \quad j_z B_x \quad -j_{phi}B_x) \tag{19}$$

$$\rho_i=\rho_{ref,i}/(1+\beta_i(T-T_{ref})) \tag{20}$$

$$\rho_{pos}=\frac{x_{Li}M_{Li}+(1-x_{Li})M_{Bi}}{(x_{Li}{}^{0.94}M_{Li}/\rho_{Li}+(1-x_{Li})^{1.64}M_{Bi}/\rho_{Bi})} \tag{21}$$

$$\boldsymbol{K}=(\mu+\mu_t)(\nabla\boldsymbol{u}+(\nabla\boldsymbol{u})^T) \tag{22}$$

$$\mu_t=\rho C_\mu\frac{k_t^2}{\varepsilon} \tag{23}$$

$$\rho\frac{\partial k_t}{\partial t}+\rho(\boldsymbol{u}\cdot\nabla)k_t=\nabla\cdot\left[\left(\mu+\frac{\mu_t}{\sigma_k}\right)\nabla k_t\right]+P_k-\rho\varepsilon \tag{24}$$

$$\rho\frac{\partial \varepsilon}{\partial t}+\rho(\boldsymbol{u}\cdot\nabla)\varepsilon=\nabla\cdot\left[\left(\mu+\frac{\mu_t}{\sigma_\varepsilon}\right)\nabla\varepsilon\right]+C_1\rho S\varepsilon -C_2\frac{\rho\varepsilon^2}{k+\sqrt{\nu\varepsilon}} \tag{25}$$

In Eq. 17-18, ρ is the density. The material's density decreases with increasing temperature (Eq. 20, where i represents Li, salt, or Bi). The density of the positive electrode depends not only on temperature but also on composition (Vegard's Law, Eq. 21). In Eq. 17, $\boldsymbol{I}$ is the identity matrix, $\boldsymbol{g}$ is the acceleration of gravity, $\boldsymbol{f}_L$ is the Lorentz force. As shown in Eq. 19, we assume that the magnetic field has only the x direction component. The expression for $\boldsymbol{K}$ is given by Eq. 22. Here, μ is viscosity (Table 1), μ_t is turbulent viscosity (Eq. 23). In Eq. 23, k_t is turbulent kinetic energy (calculated by Eq. 24), and ε is the turbulent dissipation rate (calculated by Eq. 25). In Eq. 23-25, σ_k = 1, σ_ε = 1.2, C_2 = 1.9, A_0 = 4. The determination of C_1 and C_μ can be referred to [28].

Table 1. Material properties

Property	Unit	Li	LiCl-KCl	Bi
ρ_{ref}	g cm^{-3}	0.4913	1.648	9.843
β	10^{-4} K^{-1}	1.80	3.20	1.24
c_p	J kg^{-1} K^{-1}	4237	1330	136
ν	10^{-7} m s^{-2}	7.13	19.8	1.33
k	W m^{-1} K^{-1}	51.9	0.69	14.2
σ	10^5 S m^{-1}	27.25	0.0015	7.19

Boundary conditions for the flow field are as follows: the left boundary is subject to axisymmetric conditions, the positive electrode-electrolyte interface is defined as a fluid-fluid interface, and all other boundaries are no-slip.

3.3 Model validation

Due to the inability to measure the internal flow velocity in liquid metal batteries, in this study, we validate the model by comparing experimental discharge curves with simulated discharge curves. Fig. 2b illustrates the comparison of discharge curves under different external magnetic field strengths (20 mT and 50 mT). It can be observed that the experimental and simulated values exhibit a high degree of similarity, with a voltage error not exceeding 2%, indicating the accuracy of the model.

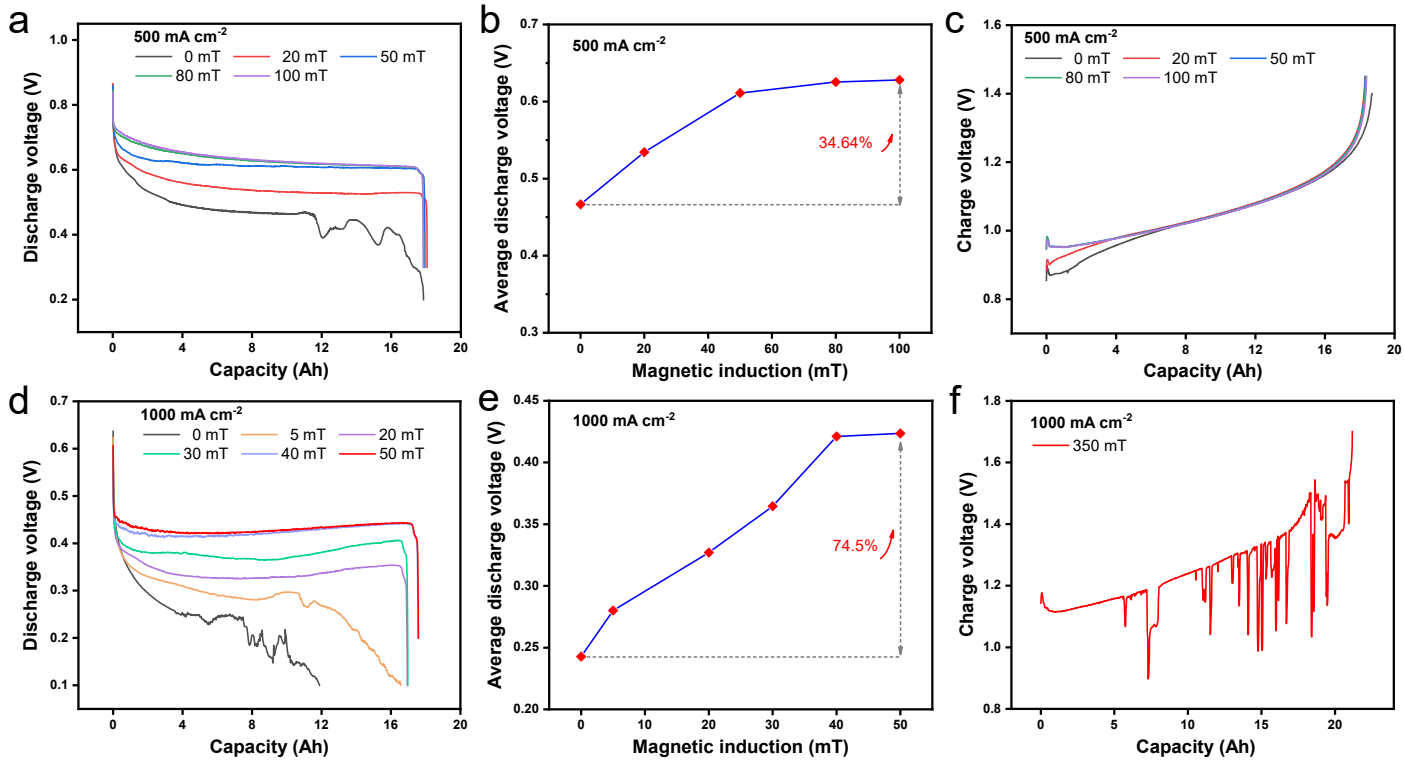

Fig. 3. (a) Discharge curves under different magnetic inductions (500 mA cm^{-2}). (b) Average discharge voltage under different magnetic inductions (500 mA cm^{-2}). (c) Charge curves under different magnetic inductions (500 mA cm^{-2}). (d) Discharge curves under different magnetic inductions (1000 mA cm^{-2}). (e) Average discharge voltage under different magnetic inductions (1000 mA cm^{-2}). (f) Charge curves under 1000 mA cm^{-2}, 350 mT.

4. RESULTS AND DISCUSSION

4.1 The effects of external magnetic fields

Fig. 3a illustrates the discharge curves of the Li|LiCl-KCl|Bi battery under different magnetic inductions (discharge current density: 500 mA cm^{-2}). In the absence of an external magnetic field (0 mT), although the battery can deliver its full capacity, there is significant fluctuation in the discharge curve in the late discharge process. This is attributed to insufficient mass transfer rate in the positive electrode, leading to the accumulation of discharge products at the interface. When a 20 mT magnetic field is applied, the voltage fluctuation in the late discharge process is eliminated. The discharge curve becomes very smooth, and the voltage is further increased. Continuing to increase the external magnetic field intensity results in a further enhancement of the discharge voltage, but beyond 80 mT, there is no substantial improvement. Fig. 3b presents the average discharge voltage under different magnetic inductions (discharge current density: 500 mA cm^{-2}). Compared to the case without an external magnetic field, the average discharge voltage under 100 mT has increased by 34.64%. When calculated in terms of discharge energy, the enhancement reaches an impressive 37.94%.

In Fig. 3c, the charge curves under different magnetic fields are presented. It can be observed that the charge curves exhibit no significant differences. According to the literature, during the charge process, vigorous solutal convection spontaneously occurs in the positive electrode, enhancing mass transfer sufficiently. Therefore, there is no need for an external magnetic field during the charge process.

Fig. 3d shows the discharge curves under different magnetic inductions at 1000 mA cm^{-2}. Without an external magnetic field, the battery cannot deliver its full capacity. When a 5 mT external magnetic field is applied, the battery can release its full capacity. Increasing the external magnetic field to 20 mT results in remarkably smooth discharge curves. However, when the magnetic induction exceeds 40 mT, the discharge curves remain essentially unchanged. At higher current densities, the effects of the external magnetic field become more pronounced. Compared to no magnetic field, the battery exhibits a 74.5% increase in discharge voltage under 50 mT, and the discharge energy under 50 mT is 2.67 times that of 0 mT. Further experiments reveal that at a current density of 1000 mA cm^{-2}, when the applied magnetic induction exceeds 350 mT, the battery operation will be unstable. As shown in Fig. 4f, the charge curve becomes

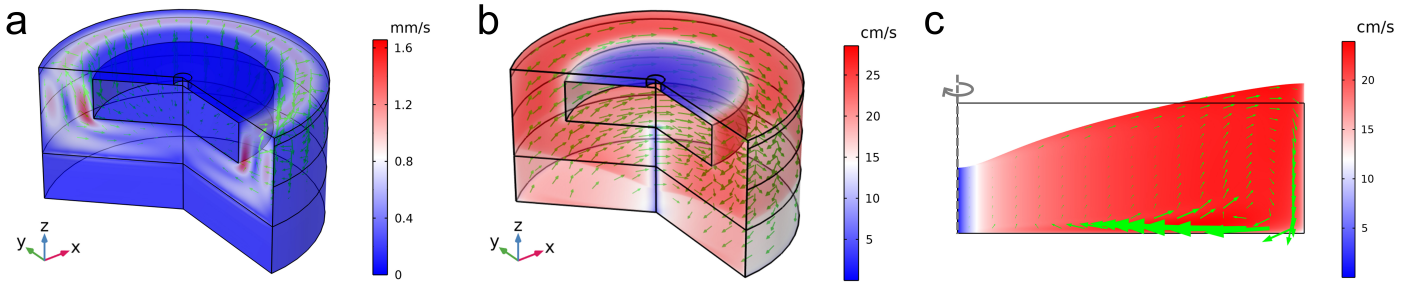

Fig. 4. (a) Flow field under 0 mT. (b) Flow field under 50 mT.
(c) Deformation of the positive electrode under 50 mT (current density: 500 mA cm^{-2}).

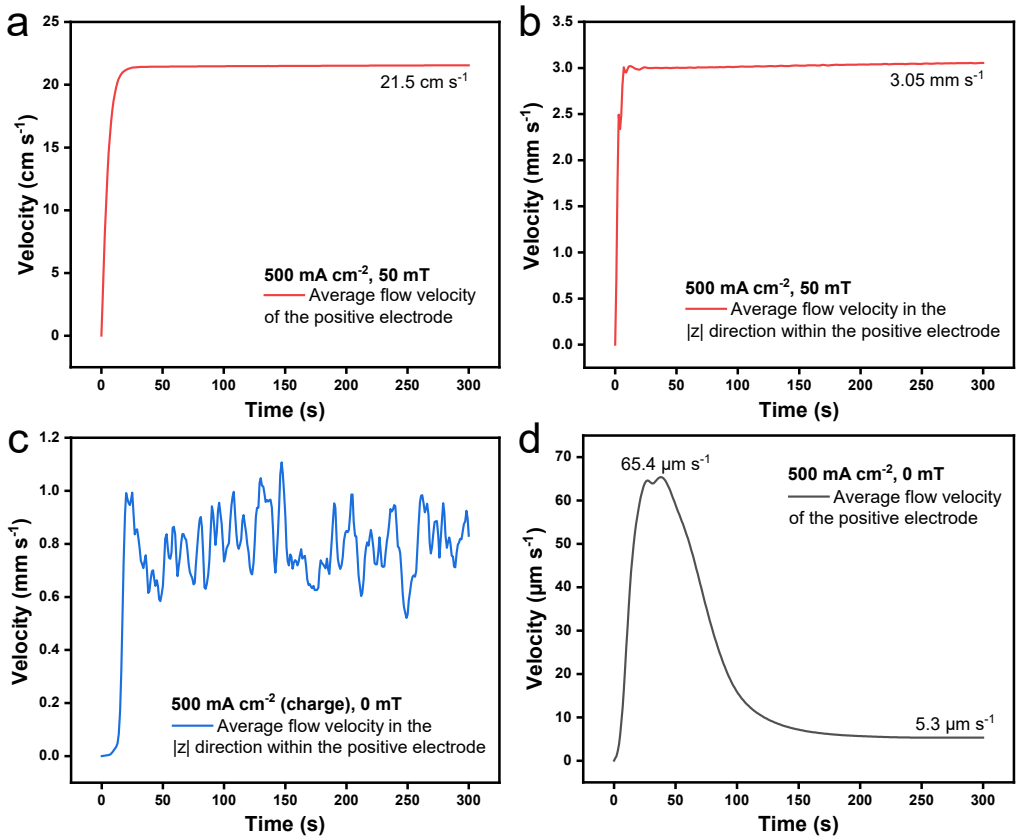

Fig. 5. (a) Average flow velocity of the positive electrode under 50 mT. (b) Average flow velocity in the |z| direction within the positive electrode under 50 mT. (c) Average flow velocity in the |z| direction within the positive electrode during charging process. (d) Average flow velocity of the positive electrode under 0 mT.

highly erratic, indicating the occurrence of circuits. Please note that such instability is more likely to occur during the charge process due to the flow suppression effect during the discharge process. However, encountering such a high magnetic induction is difficult, and we will investigate this phenomenon in subsequent research.

Based on the above discussions, the following conclusions can be drawn: (1) External magnetic fields have a significant enhancing effect on the discharge performance of LMBs. (2) External magnetic fields have a relatively minor impact on the charge performance. (3) Very high current densities and magnetic inductions will cause the operation instability.

4.2 Mechanism

Using simulation software (COMSOL), we simulated the fluid flow and mass transfer inside the liquid metal battery. As shown in Fig. 4a, in the absence of an external magnetic field, there is internal heating flow in the molten salt electrolyte [24,29]. This is because the conductivity of the molten salt electrolyte is low (2-3 orders of magnitude lower than the positive and negative metal), leading to substantial Joule heating during discharge and generating thermal convection. The

maximum flow velocity in the molten salt is approximately 1.6 mm s^{-1}. Due to the high conductivity of the positive electrode and the stable density stratification during discharge, there is essentially no flow in the positive electrode.

When a 50 mT magnetic field is applied, the magnetic induction ***B*** in the x direction interacts with the current (***J***) in -z direction, generating a Lorentz force in the azimuthal (phi) direction. This induces a swirling flow within the battery, as illustrated in Fig. 4b. The velocity of the swirling flow is extremely fast, exceeding 25 cm s^{-1}, rendering the internal heating flow in the molten salt negligible. Furthermore, the rapid swirling flow causes deformation in the fluid domain, resulting in a morphology where the positive electrode exhibits a lower central region surrounded by higher regions (Fig. 4c). However, due to the presence of a certain distance between the positive and negative electrodes (Fig. 2a), this deformation is insufficient to cause instability in the operation of the battery.

It is worth noting that the flow in the phi direction does not assist in the transport of Li atoms within the positive electrode. The truly effective flow is in the |z| direction, aiding the transport of Li from the electrode-electrolyte interface to the bulk of positive electrode. However, due to the extremely fast velocity of the swirling flow, the flow within the LMB has long transitioned from laminar to turbulent. The presence of turbulence ensures the existence of a certain degree of |z| direction (including the z and -z directions) flow within the positive electrode.

As shown in Fig. 5a, under the application of a 50 mT external magnetic field, the average flow velocity in the positive electrode reaches 21.5 cm s^{-1}. Due to the presence of turbulence, the average flow velocity in the |z| direction reaches 3.05 mm s^{-1} (Fig. 5b). For comparison, during the charging process, intense solutal convection occurs in the positive electrode of LMBs, significantly reducing concentration polarization, but the average flow velocity in |z| direction is only around 0.8 mm s^{-1} (Fig. 5c). Therefore, although the primary direction of the swirling flow is in the azimuthal phi direction, its |z| directional component is sufficient to significantly reduce concentration polarization and enhance the discharge performance. Fig. 5d illustrates the evolution of flow velocity without an external magnetic field (0 mT), showing that the flow velocity in the positive electrode during discharge process is negligible, at only 5.3 μm s^{-1}.

Fig. 6a illustrates the evolution of Li concentration at the positive electrode-electrolyte interface under

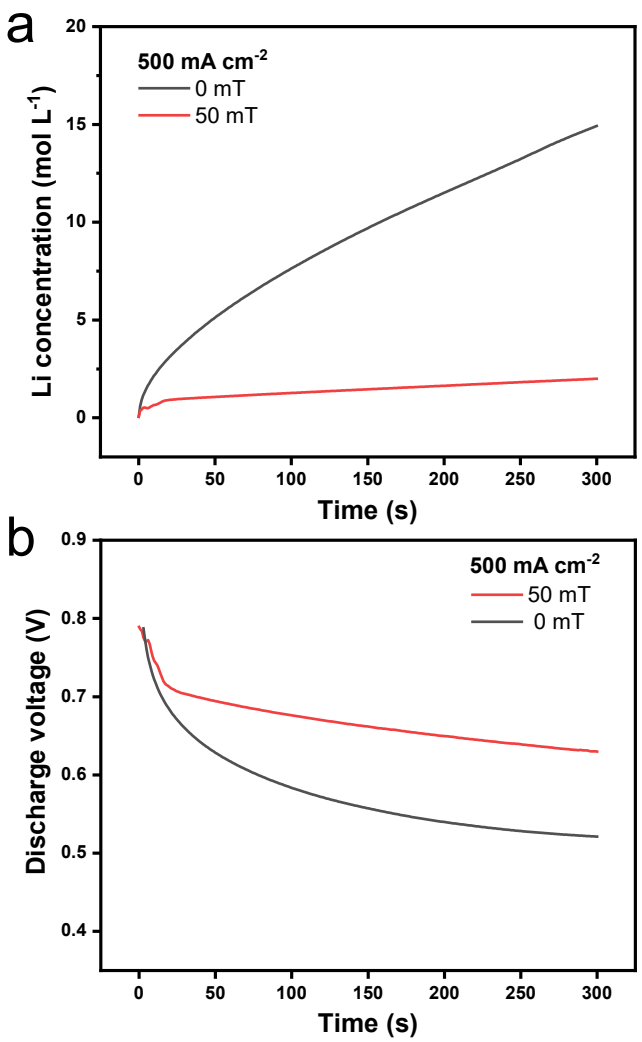

Fig. 6. (a) Variation of Li concentration at the positive electrode-electrolyte interface under 0 mT and 50 mT (b) Discharge curves under 0 mT and 50 mT

external MF (50 mT) and no MF (0 mT). It is observed that the Li concentration at the interface is significantly lower under 50 mT compared to 0 mT. This is attributed to the flow generated by the external magnetic field, particularly the |z| directional flow, aiding in the transport of Li atoms from the interface to the positive electrode bulk. A lower interfacial Li concentration implies reduced concentration polarization (Eq. 1-2). Consequently, the discharge voltage of the battery under 50 mT is notably higher than that under 0 mT (Fig. 6b).

5. CONCLUSIONS

In this study, we established, for the first time, an experimental platform for applying external magnetic fields to liquid metal batteries. We measured the charge/discharge performance of the Li|LiCl-KCl|Bi battery under the influence of external magnetic fields. The experiments revealed a significant enhancement in the discharge performance of the LMB due to the

external magnetic field, particularly at high current densities, while its influence on the charging performance was relatively minor. A multi-field coupled model, incorporating electrochemical reactions, mass transfer, and fluid flow, was developed using COMSOL software to elucidate the underlying mechanisms. The fluid inside the battery generated swirling flow in the azimuthal direction under the influence of Lorentz forces, transitioning to turbulent flow with a certain |z| directional velocity when the flow rate was sufficiently high. This turbulence effectively reduced concentration polarization at the positive electrode-electrolyte interface, thereby increasing the discharge voltage of the battery.

In subsequent work, methods such as the design of the positive electrode current collector can be employed to enhance the |z| directional flow, thereby reducing the required external MF intensity. When combined with low-temperature LMB systems [23], permanent magnets capable of operating at temperatures between 300 to 350 ^{o}C can replace Helmholtz coils, facilitating the application of external magnetic field technology in LMB modules [30].

ACKNOWLEDGEMENT

This work was supported by the National Natural Science Foundation of China (Grant No. 52177215, 52277217).

DECLARATION OF INTEREST STATEMENT

The authors declare that they have no known competing financial interests or personal relationships that could have appeared to influence the work reported in this paper.

REFERENCE

[1] Zhu Z, Jiang T, Ali M, Meng Y, Jin Y, Cui Y, et al. Rechargeable Batteries for Grid Scale Energy Storage. Chem Rev 2022;122:16610–751.

[2] Zhou X, Xie H, He X, Zhao Z, Ma Q, Cai M, et al. Annihilating the Formation of Silicon Carbide: Molten Salt Electrolysis of Carbon–Silica Composite to Prepare the Carbon–Silicon Hybrid for Lithium-Ion Battery Anode. ENERGY & ENVIRONMENTAL MATERIALS 2020;3:166–76.

[3] Ning X, Phadke S, Chung B, Yin H, Burke P, Sadoway DR. Self-healing Li–Bi liquid metal battery for grid-scale energy storage. Journal of Power Sources 2015;275:370–6.

[4] Kim H, Boysen DA, Newhouse JM, Spatocco BL, Chung B, Burke PJ, et al. Liquid Metal Batteries: Past, Present, and Future. Chem Rev 2013;113:2075–99.

[5] Li H, Shen Y, Zhang Z, Cheng A, Wang K, Zhou X, et al. The interfacial engineering of metal electrodes for high-specific-energy and long-lifespan batteries. iEnergy 2022;1:204–22.

[6] Xia J, Shi Q, Li H, Zhou M, Wang W, Wang K, et al. Historical data-independent remaining useful life prediction method based on dual-input deep learning neural network. Journal of Energy Storage 2023;72:108427.

[7] Li H, Yin H, Wang K, Cheng S, Jiang K, Sadoway DR. Liquid Metal Electrodes for Energy Storage Batteries. Advanced Energy Materials 2016;6:1600483.

[8] Wang K, Jiang K, Chung B, Ouchi T, Burke PJ, Boysen DA, et al. Lithium–antimony–lead liquid metal battery for grid-level energy storage. Nature 2014;514:348–50.

[9] Zhou X, Zhou H, Yan S, He Y, Zhang W, Li H, et al. Increasing the actual energy density of Sb-based liquid metal battery. Journal of Power Sources 2022;534:231428.

[10] Zhou H, Li H, Gong Q, Yan S, Zhou X, Liang S, et al. A sodium liquid metal battery based on the multi-cationic electrolyte for grid energy storage. Energy Storage Materials 2022;50:572–9.

[11] Liu G, Xu C, Li H, Jiang K, Wang K. State of charge and online model parameters co-estimation for liquid metal batteries. Applied Energy 2019;250:677–84.

[12] Xu C, Zhang E, Jiang K, Wang K. Dual fuzzy-based adaptive extended Kalman filter for state of charge estimation of liquid metal battery. Applied Energy 2022;327:120091.

[13] Weber N, Galindo V, Stefani F, Weier T. Current-driven flow instabilities in large-scale liquid metal batteries, and how to tame them. Journal of Power Sources 2014;265:166–73.

[14] Kelley DH, Weier T. Fluid Mechanics of Liquid Metal Batteries. Applied Mechanics Reviews 2018;70.

[15] Agarwal D, Potnuru R, Kaushik C, Darla VR, Kulkarni K, Garg A, et al. Recent advances in the modeling of fundamental processes in liquid metal batteries. Renewable and Sustainable Energy Reviews 2022;158:112167.

[16] Personnettaz P, Landgraf S, Nimtz M, Weber N, Weier T. Mass transport induced asymmetry in charge/discharge behavior of liquid metal batteries. Electrochemistry Communications 2019; 105:106496.

[17] Personnettaz P, Klopper TS, Weber N, Weier T. Layer coupling between solutal and thermal convection in liquid metal batteries. International Journal of Heat and Mass Transfer 2022;188:122555.

[18] Herreman W, Bénard S, Nore C, Personnettaz P, Cappanera L, Guermond J-L. Solutal buoyancy and electrovortex flow in liquid metal batteries. Phys Rev Fluids 2020;5:074501.

[19] Zhou X, Gao C, Shen Y, Li H, Yan S, Zhou H, et al. Multi-field coupled model for liquid metal battery: Comparative analysis of various flow mechanisms and their effects on mass transfer and electrochemical performance. Energy Reports 2022;8:5510–21.

[20] Herreman W, Nore C, Cappanera L, Guermond J-L. Efficient mixing by swirling electrovortex flows in liquid metal batteries. Journal of Fluid Mechanics 2021;915:A17.
[21] Davidson PA, Wong O, Atkinson JW, Ranjan A. Magnetically driven flow in a liquid-metal battery. Phys Rev Fluids 2022;7:074701.
[22] Keogh DF, Baldry M, Timchenko V, Reizes J, Menictas C. Modelling the effects of areal capacity on mass transport in liquid metal batteries. Journal of Power Sources 2023;573:233142.
[23] Zhou X, Yan S, He X, Zhou H, Ning J, Li H, et al. Low-Temperature, High Cycling Stability, and High Coulombic Efficiency Liquid Metal Batteries Enabled by Lithium Halide-Potassium Halide Molten Salt Electrolytes. Energy Storage Materials 2023:102889.
[24] Personnettaz P, Beckstein P, Landgraf S, Köllner T, Nimtz M, Weber N, et al. Thermally driven convection in Li||Bi liquid metal batteries. Journal of Power Sources 2018;401:362–74.
[25] Weber N, Duczek C, Horstmann GM, Landgraf S, Nimtz M, Personnettaz P, et al. Cell voltage model for Li-Bi liquid metal batteries. Applied Energy 2022;309:118331.
[26] Zhang Y, Zhang E, Guo Z, He X, He Y, Li H, et al. Numerical study on thermal characteristics under external short circuit for Li||Bi liquid metal batteries. Applied Energy 2023;348:121480.
[27] Walz M-M, van der Spoel D. Direct Link between Structure, Dynamics, and Thermodynamics in Molten Salts. J Phys Chem C 2019;123:25596–602.
[28] Chakchak S, Hidouri A, Ghabi A, Chrigui M, Boushaki T. Numerical Study of Turbulent Swirling Diffusion Flame Under Lean and Rich Conditions Using Turbulence Realizable k-epsilon Model. Combustion Science and Technology 2023;195:1461–82.
[29] Zhou X, Gao C, Wang K, Jiang K, Li H. A Comparative Study of Thermally and Electromagnetically Driven Flow in the Electrolyte of Liquid Metal Batteries and Their Effects on Ion Transport. IEEE Transactions on Industry Applications 2023:1–9.
[30] Zhang E, Xu C, Wang S, Shi Q, Zhang Y, Li H, et al. Effects of cell-to-cell variations on series-connected liquid metal battery pack capacity. Journal of Energy Storage 2023;73:109148.